



Cite this: *RSC Adv.*, 2025, 15, 25393

# Ti<sub>3</sub>C<sub>2</sub>T<sub>x</sub> MXene embedded with nickel-molybdenum sulfide for a high-performance hydrogen evolution reaction in alkaline media†

Shaista Zubaid,<sup>a</sup> Misbah Jabeen,<sup>a</sup> Hirra Ahmad,<sup>a</sup> Abid Ur Rehman Chaudhary,<sup>a</sup> Syed Ali Raza Naqvi,<sup>b</sup> Aliya Tufail,<sup>a</sup> Atta Ullah Shah,<sup>c</sup> Yaqoob Khan<sup>\*d</sup> and Tauqir A. Sherazi<sup>†</sup> 

Transition-metal chalcogenides have emerged as strong candidates for the hydrogen evolution reaction (HER) due to their exceptional catalytic activity. A facile synthetic method of Ti<sub>3</sub>C<sub>2</sub>T<sub>x</sub> MXene, and transition-metal chalcogenides (specifically nickel-molybdenum sulfide), and their hybrid formation *via in situ* growth of nickel-molybdenum sulfide within MXene 2D nanosheets (NiMo<sub>3</sub>S<sub>4</sub>-MXene) is reported. The synthesis of these electrocatalysts was confirmed through X-ray diffraction spectroscopy (XRD), scanning electron microscopy (SEM), and energy-dispersive X-ray spectroscopy (EDS). Electrochemical studies of NiMo<sub>3</sub>S<sub>4</sub> and NiMo<sub>3</sub>S<sub>4</sub>-MXene were conducted after depositing these materials onto nickel foam, which served as the "current collector". The HER performance of NiMo<sub>3</sub>S<sub>4</sub> was significantly enhanced in an alkaline medium after forming a hybrid with MXene (NiMo<sub>3</sub>S<sub>4</sub>-MXene). The overpotential was found to be 104 mV at 10 mA cm<sup>-2</sup>, and the Tafel slope for the HER was 52 mV dec<sup>-1</sup>. NiMo<sub>3</sub>S<sub>4</sub>-MXene exhibited remarkable durability and a low charge-transfer resistance ( $R_{ct} = 2.18 \Omega$ ). The high electrical conductivity of MXene ensured efficient electron transport to active sites, whereas NiMo<sub>3</sub>S<sub>4</sub> offered excellent catalytic activity, facilitating proton adsorption and hydrogen generation. Thus, a synergistic effect arises from the complementary properties of the components in the hybrid electrocatalyst, resulting in favourable characteristics for the HER. These findings suggest that the transition-metal chalcogenides, in combination with MXene, could serve as efficient and durable electrocatalysts for electrochemical water-splitting.

Received 25th April 2025  
Accepted 1st July 2025

DOI: 10.1039/d5ra02903a

rsc.li/rsc-advances

## 1 Introduction

It is well established that the development of sustainable energy resources is essential to meet the growing demand for energy. In this context, renewable energy resources show great potential to satisfy energy requirements.<sup>1</sup> However, there is still need to achieve low cost, efficient, and clean energy alternatives.

Hydrogen fuel is considered one of the most promising non-carbonaceous, environmentally friendly energy carriers.<sup>2,3</sup> Water-splitting is an emerging technique for hydrogen

production, requiring an ideal potential of 1.23 V to split water into hydrogen and oxygen gases. In practice, this potential reaches up to 1.8 V, which is quite high and makes the thermodynamic process expensive.<sup>4,5</sup> The efficiency of water-splitting is limited due to inevitable kinetic overpotentials. These overpotentials can be minimized by applying efficient electrocatalysts. Noble metal-based electrocatalysts, such as Pt/C, are commonly used for the hydrogen evolution reaction (HER) *via* electrochemical water-splitting.<sup>6,7</sup> Although Pt/C exhibits excellent performance in both acidic and alkaline media, its high cost and scarcity make it unsuitable for large-scale HER applications. Therefore, there is a strong need to explore efficient yet cost-effective non-noble metal-based electrocatalysts for the HER.<sup>8,9</sup> However, non-noble metals are unstable in acidic environments; therefore, using an alkaline medium is a preferable alternative for non-noble metal-based electrocatalysts. These electrocatalysts can be rationally designed to possess high electrical conductivity, enhanced surface hydrophilicity, superior electrocatalytic activity, good structural stability, and abundant active sites.<sup>10-14</sup> In this regard, the MXene family (*e.g.*, Ti<sub>3</sub>C<sub>2</sub>, Ti<sub>2</sub>C, and V<sub>2</sub>C) has attracted considerable interest as a promising class of HER

<sup>a</sup>Department of Chemistry, COMSATS University Islamabad, Abbottabad Campus, Abbottabad 22060, Pakistan. E-mail: sherazi@cuiatd.edu.pk

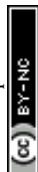
<sup>b</sup>Department of Chemistry, Government College University Faisalabad, Faisalabad 38040, Pakistan

<sup>c</sup>National Institute of Lasers and Optonics College, Pakistan Institute of Engineering and Applied Sciences, Islamabad 45650, Pakistan

<sup>d</sup>Nanosciences and Technology Department, National Centre for Physics, Islamabad 45320, Pakistan. E-mail: yaqoob@ncp.edu.pk

† Electronic supplementary information (ESI) available. See DOI: <https://doi.org/10.1039/d5ra02903a>

‡ Visiting affiliation: INM, Leibniz Institute for New Materials, Campus D2.2, 66123 Saarbrücken, Germany.



electrocatalysts due to their two dimensional (2D) morphology, excellent metallic conductivity, strong mechanical strength, and highly hydrophilic surfaces.<sup>15</sup> MXene formation relies on the etching of the MAX phase (e.g.,  $\text{Ti}_3\text{AlC}_2$ ), where various terminating groups ( $-\text{F}$ ,  $-\text{O}$  and  $-\text{OH}$ ) lead to the formation of the stable nanosheets of the corresponding MXene, such as  $\text{Ti}_3\text{C}_2\text{T}_x$  if  $\text{Ti}_3\text{AlC}_2$  is used as the MAX phase.<sup>16</sup> These ultrathin MXene sheets are prone to restacking. Therefore, it is necessary to introduce a spacer or incorporate them into a 2D or 3D framework to minimize this tendency.<sup>17–19</sup> Conversely, cost-effective transition-metal chalcogenides (TMCs)-based electrocatalysts, such as  $\text{Ni}_3\text{S}_2$ ,  $\text{NiS}$ ,  $\text{CoS}$ ,  $\text{Fe}_2\text{S}$ , and  $\text{MoS}_2$ , have been developed with promising properties, including high HER activity and abundant active sites.<sup>20</sup> A heterogeneous bimetallic sulfide/phosphide-based electrocatalyst supported on nickel foam ( $\text{NiFeSP/NF}$ ) has been reported, exhibiting remarkable activity in alkaline media with a low overpotential of 91 mV at a current density of  $10 \text{ mA cm}^{-2}$  for the HER. A few reports have also highlighted advances in bimetallic sulfide-based hybrid electrocatalysts coupled with 2D nanomaterials.<sup>21,22</sup> Additionally, a hollow Chevrel-phase  $\text{NiMo}_3\text{S}_4$ -based electrocatalyst has also been studied, offering an overpotential of 257 mV at a current density of  $10 \text{ mA cm}^{-2}$  and a Tafel slope of  $98 \text{ mV dec}^{-1}$ .<sup>23</sup> MXene-based co-catalysts, in combination with metal sulfides, such as  $\text{ZnS}$  or  $\text{Zn-CdS}$ , have exhibited enhanced water-splitting characteristics.<sup>24</sup> These encouraging results have motivated researchers to further explore MXene in combination with bimetallic sulfides. Hence, the integration of MXene sheets with TMCs or bimetallic sulfides could lead to remarkable HER performance through a synergistic effect.

Herein, we present a facile synthesis of a bimetallic sulfide ( $\text{NiMo}_3\text{S}_4$ )-based electrocatalyst and its composite with MXene ( $\text{NiMo}_3\text{S}_4$ -MXene) *via in situ* hydrothermal synthesis.  $\text{NiMo}_3\text{S}_4$ -MXene exhibited a significantly enhanced HER performance in alkaline media, as evidenced by its lower overpotential and Tafel slope values, which are very close to those of the noble metal Pt/C. The synergistic effect between titanium-carbide MXene ( $\text{Ti}_3\text{C}_2\text{T}_x$ ) and nickel-molybdenum sulfide ( $\text{NiMo}_3\text{S}_4$ ) in the HER arises from their complementary properties, significantly enhancing the overall catalytic performance. The high electrical conductivity of MXenes ensured efficient electron transport to the active sites, while  $\text{NiMo}_3\text{S}_4$  provided excellent catalytic activity by facilitating proton adsorption and hydrogen generation. The 2D layered structure of MXene increased the surface area, exposing more  $\text{NiMo}_3\text{S}_4$  active sites and promoting faster reaction kinetics. This combination also led to improved charge transfer, thereby lowering the overpotential required for the HER. Additionally, the structural stability of MXenes supported the durability of the catalyst by preventing the degradation of  $\text{NiMo}_3\text{S}_4$  in alkaline media. This synergy resulted in a highly efficient, durable, and scalable catalyst for the HER, outperforming the individual components. The large specific surface area provided by MXene in the hybrid electrocatalyst increased the exposure of  $\text{NiMo}_3\text{S}_4$  active sites, thereby boosting catalytic activity. It is anticipated that bimetallic sulfide-based hybrid electrocatalysts will open up new avenues developing other rationally designed electrochemically active

nanostructures aimed at promising applications in the field of energy storage and conversion.

## 2 Materials and methods

### 2.1 Materials

Sodium molybdate dihydrate (98.5%), nickel chloride hexahydrate ( $\geq 98\%$ ), thiourea ( $\geq 99\%$ ), cobalt chloride hexahydrate (98%), and ascorbic acid (99%) were purchased from Sigma-Aldrich. Potassium hydroxide pellets ( $\geq 85\%$ ), used as the electrolyte material, were purchased from Daejung Chemicals in Korea. Titanium aluminium carbide powder ( $>90\%$ ), HF (49%), and ethanol (99.8%) were also purchased from Sigma-Aldrich. Nickel foam (thickness = 1.6 mm) was obtained from Shanghai Tankii Alloy Materials. All reagents were of analytical grade and used as received without further purification.

### 2.2 Fabrication of MXene nanosheets

First, 2.0 g of MAX phase ( $\text{Ti}_3\text{AlC}_2$ ) was slowly added to 40 mL of hydrofluoric acid (49%). The solution was continuously stirred using a magnetic stirrer at 200 rpm for 24 h at room temperature to etch the aluminium (Al) layers from the MAX phase ( $\text{Ti}_3\text{AlC}_2$ ). All hydrofluoric acid (HF)-related reactions were conducted in a fume hood, and appropriate safety precautions were taken while handling. After etching, the reaction mixture was repeatedly washed with deionized water (DI) until the pH reached 7. The resulting product was then dried in a vacuum oven at  $60^\circ\text{C}$  overnight to obtain MXene ( $\text{Ti}_3\text{C}_2\text{T}_x$ ).

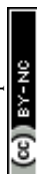
### 2.3 Preparation of electrocatalysts

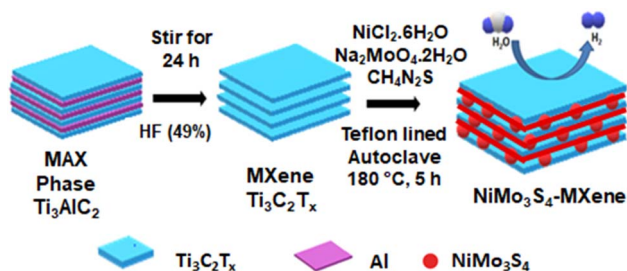
A hydrothermal method was used to prepare  $\text{NiMo}_3\text{S}_4$ . For this purpose, 0.34 mM nickel chloride hexahydrate ( $\text{NiCl}_2 \cdot 6\text{H}_2\text{O}$ ), 0.17 mM sodium molybdate dihydrate ( $\text{Na}_2\text{MoO}_4 \cdot 2\text{H}_2\text{O}$ ), and 3 mM thiourea ( $\text{CH}_4\text{N}_2\text{S}$ ) were dissolved in 25 mL of DI water. To the prepared solution, 0.8 mL of ascorbic acid was added, followed by sonication for 1 h and stirring for 30 min. The resulting solution was then transferred to a 50 mL Teflon<sup>TM</sup>-lined autoclave and heated in a drying oven at  $180^\circ\text{C}$  for 5 h. The product obtained was centrifuged at 6000 rpm for 10–15 min. The resulting black precipitate was washed several times with DI water and then with ethanol, followed by drying in a vacuum oven at  $60^\circ\text{C}$ . A solid blackish product was obtained.  $\text{NiMo}_3\text{S}_4$ -MXene was also prepared using the same hydrothermal method, where the above-mentioned precursors were used as such, and 40 mg of MXene was added and mixed with ascorbic acid solution.

The mixture was sonicated for 1 h and stirred for 30 min. The solution was then transferred to a 500 mL Teflon<sup>TM</sup>-lined autoclave, and the hydrothermal reaction was conducted at  $180^\circ\text{C}$  for 5 h. The resulting product was centrifuged, washed, and dried, following the same procedure described for the synthesis of  $\text{NiMo}_3\text{S}_4$ . Scheme 1 presents an illustration of the electrocatalyst preparation.

### 2.4 Electrode fabrication

Ni foam was used as the support surface for the deposition of the electrocatalytic material. Ni foam was selected as the



Scheme 1 Preparation of the NiMo<sub>3</sub>S<sub>4</sub>-MXene hybrid electrocatalyst.

substrate due to its unique characteristics, including 3D porous structure, large surface area, excellent electrical conductivity, robust mechanical stability, and resistance to alkaline environments. Polytetrafluoroethylene (PTFE) was used as a binder, whereas carbon black served as the conducting agent. Initially, the ratio of active material, conducting agent, and binder was taken as 8.0 mg, 1.5 mg, and 0.5 mg, respectively. The active material and conducting agent were mixed and ground using a pestle and mortar. A measured amount of PTFE dispersion was added dropwise to make a slurry. The resulting material was uniformly deposited onto a 1 cm<sup>2</sup> area of Ni foam and used as the working electrode. Before deposition of the active material, the 1 cm<sup>2</sup> area of Ni foam was carefully pressed to flatten its surface, which helps to avoid penetration of active material into the porous structure of Ni foam. This strategy also helped maintain the surface area covered with the active material at ~1 cm<sup>2</sup>. The weight of the Ni foam was measured before and after the deposition of active mass of electrocatalyst, which provided a mass loading of 3.6 mg cm<sup>-2</sup>. To determine the mass loading, the Ni foam with the deposited active material was first dried in a vacuum oven at 80 °C for ~5 h. It is recommended that the mass loading of the active material be <4.0 mg cm<sup>-2</sup> to achieve better electrochemical performance because higher mass loading lead to the formation of a thicker layer that may hinder electrolyte penetration into the electrocatalyst, potentially reducing performance.<sup>25</sup>

### 2.5 Physical and electrochemical characterizations

SEM and EDX measurements were carried out using a field-emission scanning electron microscope (FE-SEM; TESCAN MAIA-3). XRD analysis was done on D8-Discover X-ray diffractometer (Bruker). X-ray photoelectron spectroscopy (XPS) was conducted using a nanoscience instrument (Omicron, Germany) equipped with an Al K $\alpha$  X-ray (1486.7 eV) mono-energetic source operated at 300 W. For XPS, the analyzer pass energy was maintained at 20 eV. Analyzer's work function was 4.5 eV and it operated in constant analyser energy (CAE) mode, with a step size of 0.5 eV. Data acquisition was undertaken using Matrix v3.2. Data analysis was conducted with Casa XPS. To avoid sample charging effects during XPS, binding energies were calibrated using C 1s peak (284.8 eV). Electrochemical measurements were conducted in alkaline media (1.0 M KOH, pH = 14) using a three-electrode system with a Gamry instrument interface 3000 at room temperature. The as-prepared

catalyst was used as the working electrode, a platinum wire served as the counter electrode, and an Ag/AgCl electrode was used as the reference electrode.<sup>26</sup> All potential values were converted to the reversible hydrogen electrode (RHE) scale using the Nernst equation as follows:

$$E_{\text{RHE}} = E_{\text{Ag/AgCl}} + 0.059 \times \text{pH} + E_{\text{Ag/AgCl}}^{\circ} \quad (1)$$

The pH of the electrolyte (KOH) was 14, and the standard electrode potential ( $E^{\circ}$ ) of the Ag/AgCl electrode was 0.197 V vs. RHE at 25 °C. Overpotential for the HER was calculated using the following equation:

$$\eta = -E_{\text{RHE}} \quad (2)$$

Linear sweep voltammetry (LSV) was performed for the HER at a scan rate of 5 mV s<sup>-1</sup>, within a potential window of 0 to -0.677 V. To assess stability, LSV was recorded before and after 1000 cyclic voltammetry (CV) cycles at scan rate of 50 mV s<sup>-1</sup> in the same potential window. Electrochemical impedance spectroscopy (EIS) was carried out over a frequency range from 100 kHz to 0.01 Hz. The obtained data were well fitted to a constant phase element (CPE) with a diffusion circuit; using this fitting model, the charge transfer resistance and solution resistance were calculated. The electrochemically active surface area (ECSA) was estimated by calculating double-layer capacitance ( $C_{\text{dl}}$ ) using CV at different scan rates ranging from 5 mV s<sup>-1</sup> to 100 mV s<sup>-1</sup>, within a non-Faradic region. A linear slope corresponding to  $C_{\text{dl}}$  was obtained by plotting various scan speeds *versus* the difference in current density ( $\Delta j$ ) between anodic and cathodic current ( $j_{\text{anodic}} - j_{\text{cathodic}}$ ). All electrochemical studies were repeated thrice, and data represent the average of these replicates.

## 3 Results and discussion

The NiMo<sub>3</sub>S<sub>4</sub>-MXene hybrid nanostructure was prepared *via* a hydrothermal process. MXene was synthesized by etching the MAX phase with HF, during which, most of the aluminium reacted with fluorine to form AlF<sub>3</sub>, leading to the removal of aluminium from the MAX phase and leaving behind MXene. This removal of Al transformed the MAX structure into 2D MXene nanosheets with increased interlayer spacing, allowing them to disperse well in various solvents, including water. Scanning electron microscopy (SEM) images of MAX (before HF etching) and MXene (after HF etching) are shown in Fig. 1a and b, respectively. These 2D MXene nanosheets appear well-separated, indicating the complete removal of Al layers through etching. The "accordion" MXene structure was bone-dried under a vacuum at 60 °C. The dry MXene is known to be stable under ambient conditions for over a year. The sulfur-rich environment used during the preparation of the nickel-molybdenum sulfide/MXene composite was helpful in preventing MXene oxidation. MXene nanosheets have a wide range of electrochemical applications due to their high surface area, good conductivity in addition to excellent mechanical strength and high stability.<sup>16</sup> Fig. 1c represents the SEM image of the



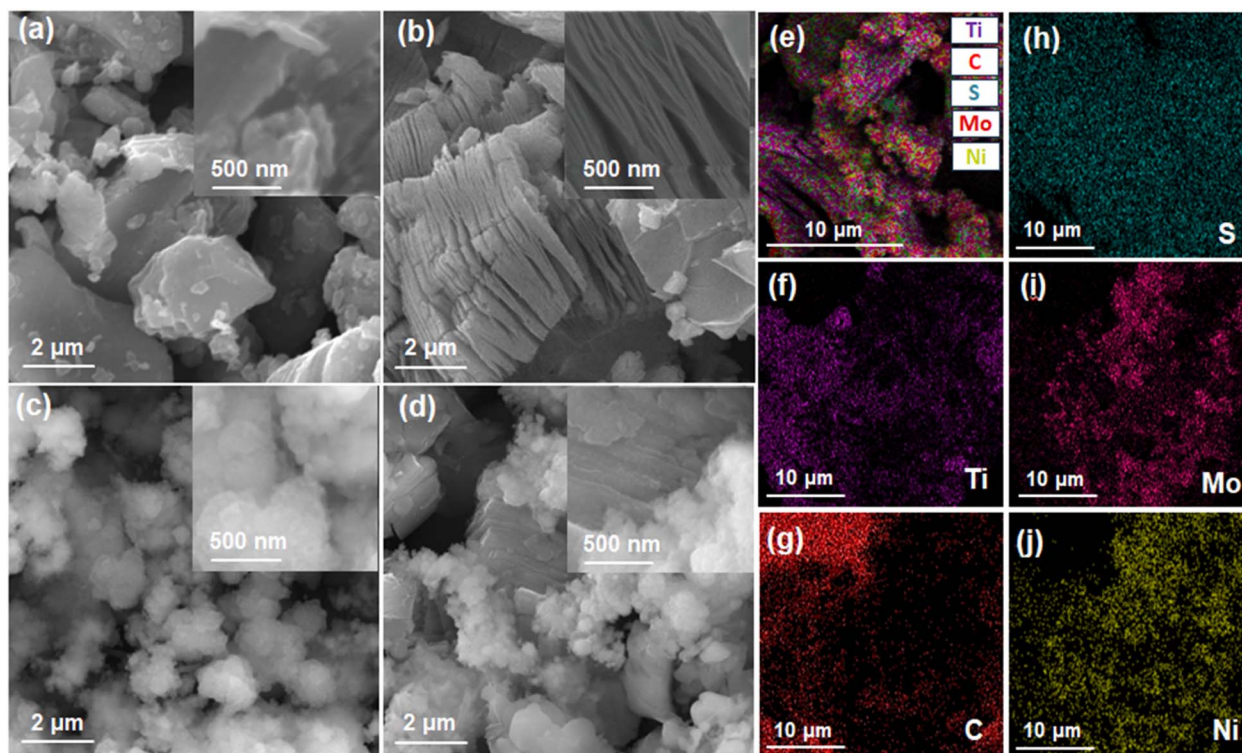


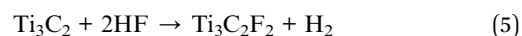
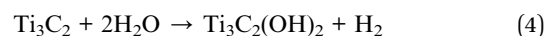
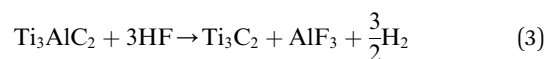
Fig. 1 SEM images of (a) titanium aluminium carbide MAX phase, (b)  $\text{Ti}_3\text{C}_2\text{T}_x$  MXene synthesized by etching of the MAX phase, (c)  $\text{NiMo}_3\text{S}_4$ , and (d)  $\text{NiMo}_3\text{S}_4$ -MXene and (e–j) EDS mapping of  $\text{NiMo}_3\text{S}_4$ -MXene.

$\text{NiMo}_3\text{S}_4$  nanostructure. The *in situ* growth of  $\text{NiMo}_3\text{S}_4$  within MXene nanosheets helped prevent restacking and promoted strong interfacial interaction between both components in the prepared  $\text{NiMo}_3\text{S}_4$ -MXene hybrid nanostructure, resulting in a synergistic enhancement of material performance (Fig. 1d). Fig. S1† also supports the growth of  $\text{NiMo}_3\text{S}_4$  within MXene 2D sheets. EDS elemental mapping of  $\text{NiMo}_3\text{S}_4$ -MXene was also performed, as presented in Fig. 1e–j. Mapping indicated that Ti, C, S, Mo, and Ni were almost uniformly distributed over the MXene surface. EDS mapping of pristine MXene and  $\text{NiMo}_3\text{S}_4$  are also provided in ESI as Fig. S2 and S3,† respectively.

Energy dispersive X-ray spectroscopy (EDS) confirmed the presence of all relevant elements in  $\text{NiMo}_3\text{S}_4$  and  $\text{NiMo}_3\text{S}_4$ -MXene, verifying the synthesis of electrocatalysts with the proposed composition. In the EDS spectrum, the abscissa represents the ionization energy, while the ordinate corresponds to counts. The EDS spectrum of the MAX phase (Fig. 2a) showed that it is composed of three main elements: titanium, aluminium, and carbon. After etching of the MAX phase with HF, the aluminium signal was significantly suppressed, indicating its removal from the structure and the subsequent formation of MXene. Etched MXene contained titanium and carbon as major elements, as shown in Fig. 2b. Fluorine was also observed as the terminal group in the EDS spectrum of MXene and originated from HF during the synthesis of MXene.

There was a possibility of the newly synthesized MXene reacting with HF, as illustrated in eqn (3)–(5). Although the reaction of MXene with water is dominant, it also reacts with

HF, resulting in the formation of  $-\text{OH}^-$  and  $-\text{F}^-$  terminal groups on the MXene surface.<sup>27</sup>



The EDX spectrum of  $\text{NiMo}_3\text{S}_4$  confirmed the presence of nickel and molybdenum metals along with sulfur (Fig. 2c). In the  $\text{NiMo}_3\text{S}_4$ -MXene hybrid structure, the elements detected were nickel, molybdenum, sulfur, titanium, and carbon, as shown in Fig. 2d. Moreover, the terminal fluorine on MXene was eliminated after its composite formation with  $\text{NiMo}_3\text{S}_4$ .

XRD analysis was performed to confirm the synthesis and determine structural information. The overlay of the XRD pattern of all samples is shown in Fig. 3. The black curve is the XRD of the MAX phase (titanium aluminium carbide), a precursor of MXene. It shows diffraction peaks at  $9.6^\circ$ ,  $19.2^\circ$ ,  $34.1^\circ$ ,  $39^\circ$ , and  $41.8^\circ$  corresponding to the (002), (004), (101), (104), and (105) crystalline planes of hexagonal  $\text{Ti}_3\text{AlC}_2$ , (JCPDS card # = 00-052-0875). After etching with HF (49%), the MAX phase was converted to MXene, as shown by the XRD pattern presented in green in Fig. 3.

The diffraction peaks appeared at  $7^\circ$ ,  $14.2^\circ$ , and  $16.8^\circ$ , corresponding to the (002), (004), and (006) planes of cubic  $\text{Ti}_3\text{C}_2\text{T}_x$  (MXene). XRD analysis provided clear confirmation that  $\text{Ti}_3\text{C}_2$



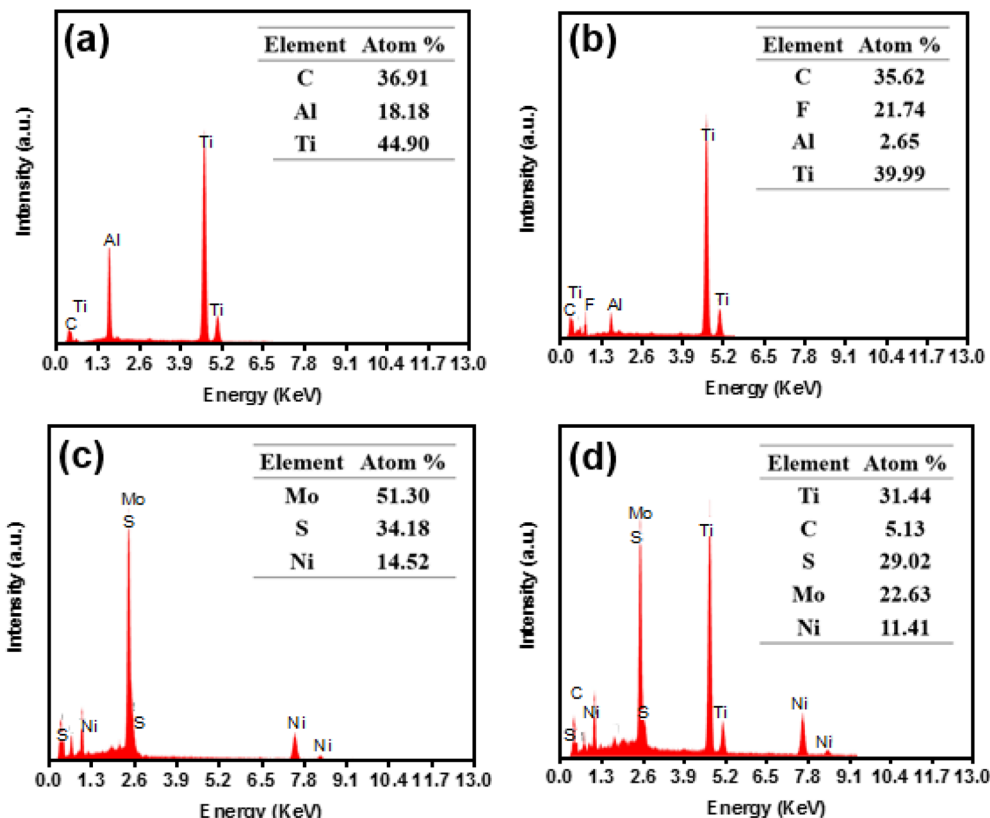


Fig. 2 EDS spectrum of (a) titanium aluminium carbide MAX phase, (b)  $\text{Ti}_3\text{C}_2\text{T}_x$  MXene synthesized by etching of the MAX phase, (c)  $\text{NiMo}_3\text{S}_4$ , and (d)  $\text{NiMo}_3\text{S}_4$ -MXene.

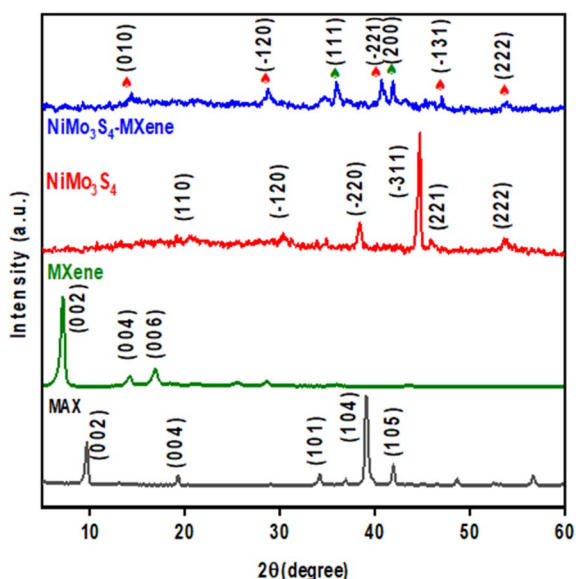


Fig. 3 X-ray diffraction pattern of the MAX phase,  $\text{Ti}_3\text{C}_2\text{T}_x$  MXene,  $\text{NiMo}_3\text{S}_4$ , and  $\text{NiMo}_3\text{S}_4$ -MXene.

MXene had been synthesized *via* etching. In particular, the transformation from the  $\text{Ti}_3\text{AlC}_2$  MAX phase to  $\text{Ti}_3\text{C}_2$  MXene was evidenced by the shifting of (002) from  $9.6^\circ$  to  $7^\circ$ . This downward shift reflects expansion of the MXene lattice and an increase in *d*-

spacing caused by the removal of aluminum and its partial replacement with  $-\text{F}$  and  $-\text{OH}$  groups during etching. Additionally, the disappearance of the characteristic Al-related peak at  $39^\circ$  further confirmed the complete removal of the Al layers from the  $\text{Ti}_3\text{AlC}_2$  precursor, which aligns with the literature.<sup>28</sup> Moreover, the absence of the  $\text{TiO}_2$  peak in the XRD pattern of MXene indicated that synthesis did not involve oxidation. The peaks appeared in the XRD curve of  $\text{NiMo}_3\text{S}_4$  at  $2\theta$  values of  $20.4^\circ$ ,  $30^\circ$ ,  $37.9^\circ$ ,  $45^\circ$ ,  $45.7^\circ$ , and  $53.8^\circ$  and were attributed to the (110), (-120), (-220), (-311), (221), and (222) planes of rhombohedral  $\text{NiMo}_3\text{S}_4$ , respectively (JCPDS card # = 01-071-0011).  $\text{NiMo}_3\text{S}_4$ -MXene showed peaks of both MXene (indicated by green leaf symbol) and  $\text{NiMo}_3\text{S}_4$  (indicated by a red leaf symbol), which confirmed the synthesis of  $\text{NiMo}_3\text{S}_4$ -MXene. Some planes of  $\text{NiMo}_3\text{S}_4$  disappeared in the composite. New peaks appeared at  $2\theta$  of  $14.2^\circ$ ,  $28.8^\circ$ ,  $40.6^\circ$ , and  $46.8^\circ$  and corresponded to the (010), (-120), (-221), and (-131) planes of rhombohedral  $\text{NiMo}_3\text{S}_4$ , respectively (JCPDS card # = 01-071-0011). Hence, some planes were suppressed while others became prominent after composite formation. It is obvious from Fig. 3 that the sharp peaks of  $\text{NiMo}_3\text{S}_4$  broadened when it combined with MXene to form the hybrid nanostructure  $\text{NiMo}_3\text{S}_4$ -MXene. The reason behind this is etching or delamination of MXene that affected the overall crystallinity of MXene nanosheets.<sup>29</sup>

X-ray photoelectron spectroscopy (XPS) was executed to investigate the surface electronic states and chemical



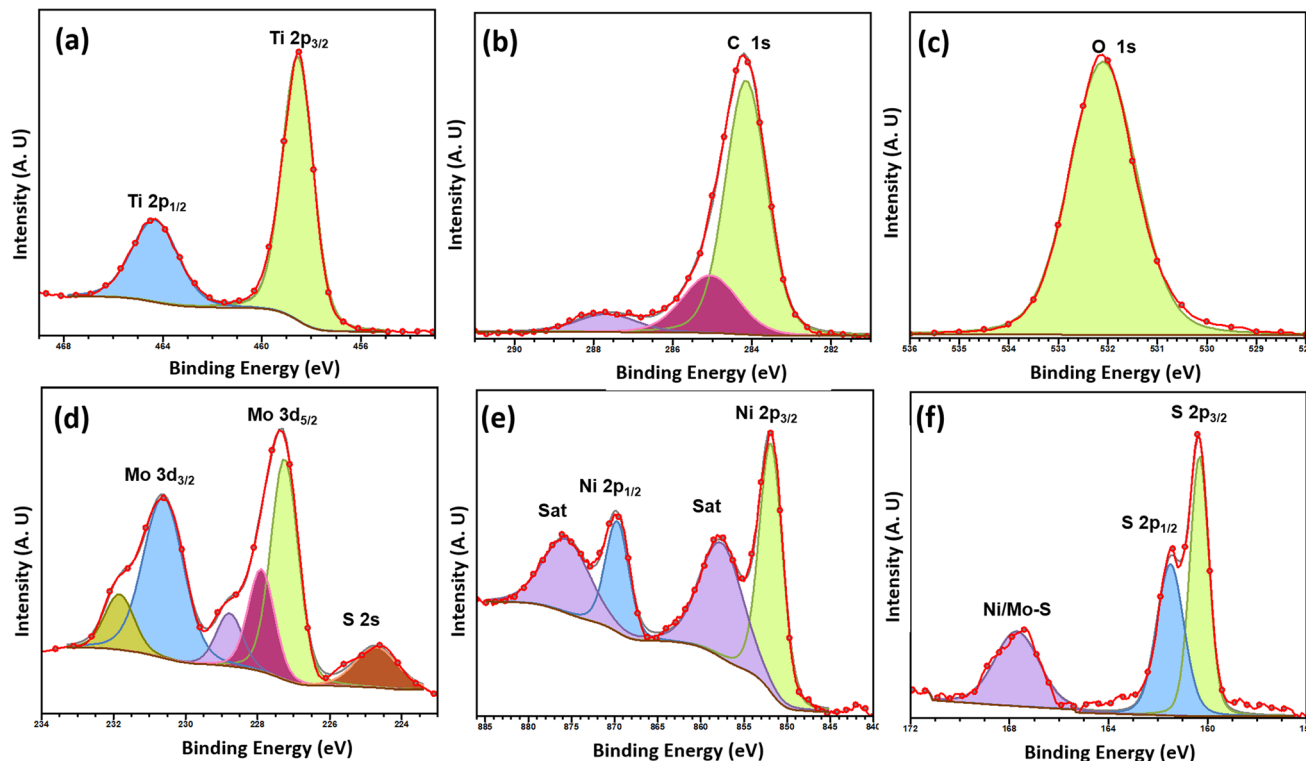


Fig. 4 XPS spectra of NiMo<sub>3</sub>S<sub>4</sub>-MXene.

composition of the NiMo<sub>3</sub>S<sub>4</sub>-MXene hybrid. XPS spectra (Fig. 4) confirmed the presence of Ti, C, O, Mo, Ni, S elements in the prepared electrode material. The XPS spectrum for Ti 2p (Fig. 4a) shows typical doublet peaks corresponding to Ti 2p<sub>3/2</sub> and Ti 2p<sub>1/2</sub>, located at binding energies (BE) of 457.6 eV and 464.5 eV, respectively.<sup>30</sup> The Ni 2p spectrum exhibited a high-energy band at of 870.6 eV for Ni 2p<sub>1/2</sub> and a low-energy band at 854.4 eV for Ni 2p<sub>3/2</sub> (Fig. 4e). Additionally, two satellite peaks at 860.3 and 873.8 eV were observed. The peaks featured at 161.2 eV and 162.8 eV (Fig. 4f) represent S 2p<sub>3/2</sub> and S 2p<sub>1/2</sub> in NiS, respectively. The partial S oxidation resulted in the appearance of one satellite peak at 168.2.<sup>31</sup>

The peaks observed in Fig. 4d at binding energies of 224.7 eV, 227.5 eV, and 231.6 eV corresponded to S 2s, Mo 3d<sub>5/2</sub>, and Mo 3d<sub>3/2</sub>, respectively, thereby confirming the presence of Mo<sup>4+</sup> in the NiMo<sub>3</sub>S<sub>4</sub>-MXene hybrid. Additionally, three peaks at 228 eV, 229 eV, and 232 eV could be attributed to MoS<sub>x</sub>O<sub>y</sub> species, indicating partial surface oxidation of MoS<sub>2</sub> due to air exposure.<sup>32</sup> MXene often contains carbon originating from the MAX-phase precursor or surface functionalization, which give rise to C 1s signal (Fig. 4b). The C 1s spectrum revealed distinct chemically shifted components, which could be deconvoluted as C=C/C-C (284 eV), C-OH (285 eV), and C=O (288 eV) (Fig. 4(b)). In Fig. 4c, the O 1s signal appears at a binding energy in the range of 530–534 eV.<sup>33</sup>

The coexistence of mixed valence states provides numerous active sites and facilitates rich redox reactions, thereby significantly enhancing the overall electrochemical performance of the hybrid electrode. These combined features make the

NiMo<sub>3</sub>S<sub>4</sub>-MXene a promising candidate for high-performance applications in overall water-splitting.

To evaluate the electrocatalytic HER performance of the prepared electrocatalysts, NiMo<sub>3</sub>S<sub>4</sub> and NiMo<sub>3</sub>S<sub>4</sub>-MXene were tested in N<sub>2</sub>-saturated 1.0 M KOH solution using the three-electrode system. In this setup, nickel foam was used as support material for depositing the active material to prepare the working electrode. For comparison, pristine Ni foam, and a working electrode prepared using pristine MXene on Ni-foam, were used with approximately the same loading as used for other electrocatalytic materials. Platinum wire was also employed as a benchmark reference for comparison. Fig. 5a shows the polarization curves of electrocatalysts obtained through linear sweep voltammetry (LSV), performed at a scan rate of 5 mV s<sup>-1</sup>. The NiMo<sub>3</sub>S<sub>4</sub>-MXene-based electrode exhibited remarkable HER activity with an onset potential of 21 mV, as compared with NiMo<sub>3</sub>S<sub>4</sub> (33 mV), MXene (46 mV), and bare NF (106 mV). Overpotential is another important parameter and direct indicator to determine the HER performance of an electrocatalyst. NiMo<sub>3</sub>S<sub>4</sub>-MXene demonstrated the lowest overpotential of 104 mV at a current density of 10 mA cm<sup>-2</sup>, outperforming the individual components used in our study (*i.e.*, NiMo<sub>3</sub>S<sub>4</sub> (241 mV) and MXene (282 mV)). Its performance approached that of Pt wire, a well-established benchmark for the HER. The overpotential of bare NF at 10 mA cm<sup>-2</sup> was also measured and found to be 397 mV.

The enhanced catalytic activity of NiMo<sub>3</sub>S<sub>4</sub>-MXene could be attributed to a synergistic effect, whereby NiMo<sub>3</sub>S<sub>4</sub> provides excellent electrocatalytic activity with the high electrical conductivity and 2D surface area of MXene. This was evidenced



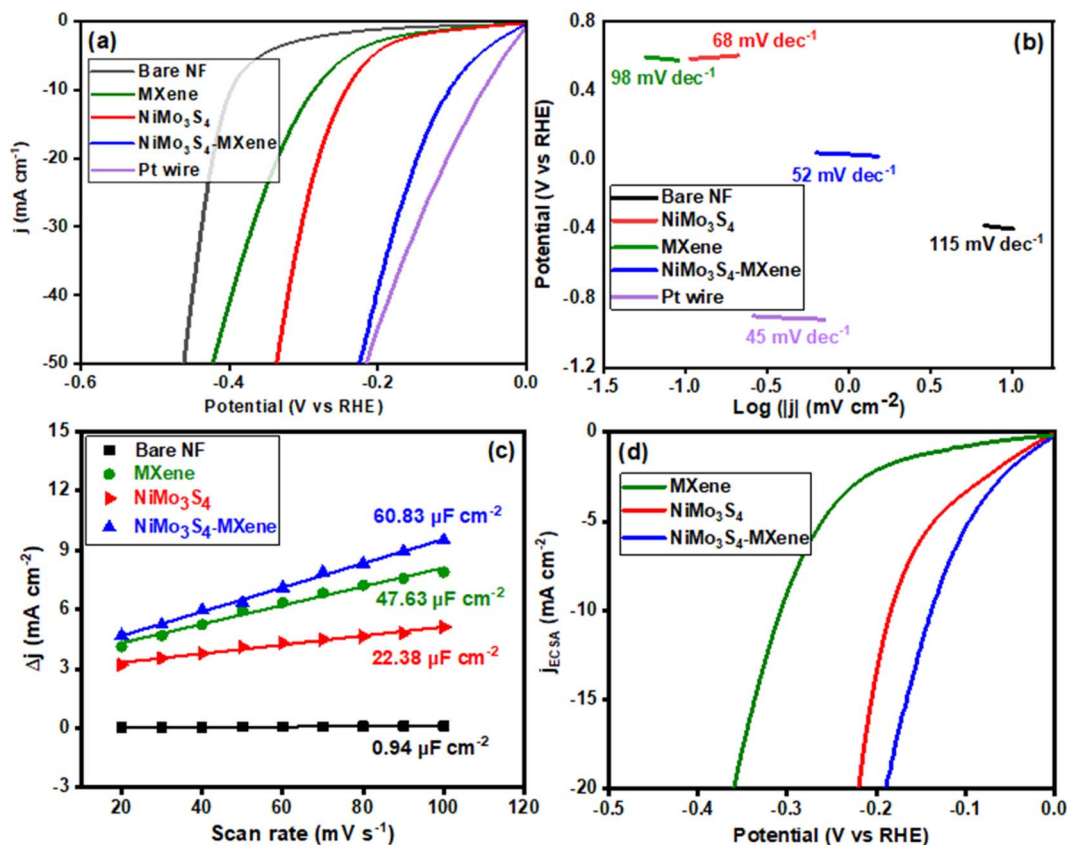


Fig. 5 (a) Polarization curves of bare Ni-foam, MXene,  $\text{NiMo}_3\text{S}_4$ ,  $\text{NiMo}_3\text{S}_4$ -MXene, and Pt wire. (b) Tafel plots of bare Ni-foam, MXene,  $\text{NiMo}_3\text{S}_4$ ,  $\text{NiMo}_3\text{S}_4$ -MXene, and Pt wire. (c)  $C_{dl}$  estimation of bare Ni-foam, MXene,  $\text{NiMo}_3\text{S}_4$ , and  $\text{NiMo}_3\text{S}_4$ -MXene. (d) Polarization curves normalized by ECSA of MXene,  $\text{NiMo}_3\text{S}_4$ , and  $\text{NiMo}_3\text{S}_4$ -MXene.

by a significant reduction in both overpotential and onset potential, indicating improved catalytic performance. As a result, more active sites are exposed, which effectively promotes the HER.<sup>34,35</sup> The significantly enhanced HER activity of  $\text{NiMo}_3\text{S}_4$ -MXene indicated that the designed electrocatalyst performed comparably with, or even better than, several other non-noble metals-based electrocatalysts (Table S2†). Pt/C was used as the noble metal-based reference electrocatalyst and exhibited excellent HER performance, with an onset potential of 14 mV, a value not yet achieved by non-noble metal electrocatalysts. However, replacing the noble metal with non-noble metals exhibiting a comparable performance is a key objective in advancing technology for widespread applications.

Fig. 5b presents the Tafel plots corresponding to polarization curves. The enhanced HER kinetics of  $\text{NiMo}_3\text{S}_4$ -MXene was supported by examining the Tafel slope.  $\text{NiMo}_3\text{S}_4$ -MXene exhibited a low Tafel slope of  $52 \text{ mV dec}^{-1}$ , which was superior to those of individual components ( $\text{NiMo}_3\text{S}_4$  ( $68 \text{ mV dec}^{-1}$ ) and MXene ( $98 \text{ mV dec}^{-1}$ )). The small Tafel slope value of  $\text{NiMo}_3\text{S}_4$ -MXene suggested the presence of more active sites and indicated a rapid increase in the hydrogen generation rate along with applied overpotential. This finding is consistent with the high activity observed in its polarization curve.

MXene notably enhances catalytic kinetics due to its metallic conductivity and water-interactive terminations ( $\pm\text{O}$ ,  $-\text{F}$ ,  $-\text{OH}$ ),

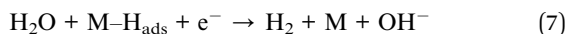
which facilitate rapid electron transport at the catalyst-electrolyte interface and promote efficient proton adsorption. For instance, recent work on alkaline  $\text{Ti}_3\text{C}_2$  MXene-based catalysts demonstrated significantly improved HER current densities and reduced overpotentials, underscoring their role in accelerating reaction rates. Its 2D structure and tunable terminal chemistry also increase active-site exposure and electrolyte penetration, collectively boosting HER kinetics.<sup>36–38</sup>

According to classical theory, the HER in alkaline media proceeds through two main steps (eqn (6)–(8)). The first step involves electron transfer leading to adsorbed hydrogen *via* water dissociation and is known as the Volmer step. The second step can proceed in two ways to produce one hydrogen molecule. If the surface coverage of adsorbed hydrogen content on the electrode is low, another  $\text{H}_2\text{O}$  molecule acquires an electron and reacts with the adsorbed hydrogen to produce molecular hydrogen (Heyrovsky step). In contrast, if the surface coverage of adsorbed hydrogen content is sufficiently high, direct coupling takes place between two adsorbed hydrogen to give molecular hydrogen (Tafel step).<sup>39</sup> Therefore, the HER follows a Volmer–Heyrovsky or Volmer–Tafel mechanism as per the following equations.

Volmer step:



Heyrovsky step:



Tafel step:



Typically, Tafel slopes of 120, 40, 30 mV dec<sup>-1</sup> correspond to the Volmer, Heyrovsky, and Tafel rate-determining steps, respectively. The Tafel slope determines the rate-limiting step in HER kinetics, with a lower slope indicating a faster HER reaction rate. The Tafel slope of the NiMo<sub>3</sub>S<sub>4</sub>-MXene was measured to be 52 mV dec<sup>-1</sup>, which was higher than that of the noble metal-based electrocatalyst Pt/C (30 mV dec<sup>-1</sup>), but lower than that of pristine MXene (98 mV dec<sup>-1</sup>) and NiMo<sub>3</sub>S<sub>4</sub> (68 mV dec<sup>-1</sup>). This result indicated that the superior HER reaction kinetics of NiMo<sub>3</sub>S<sub>4</sub>-MXene were through the water-dissociation reaction and followed the Volmer–Heyrovsky mechanism for hydrogen production, whereas Heyrovsky was the rate-determining step. The overpotential values of all prepared electrocatalysts at specific current densities (10, 50, 100 and 200 mA cm<sup>-2</sup>) are presented in Fig. S4.† NiMo<sub>3</sub>S<sub>4</sub>-MXene exhibited the lowest overpotential (104 mV) at a current density of 10 mA cm<sup>-2</sup>.

To further explore the catalytic activity of designed electrocatalysts, the ECSA was measured, which is proportional to the double-layer capacitance (*C*<sub>dl</sub>). Using *C*<sub>dl</sub>, the ECSA of NiMo<sub>3</sub>S<sub>4</sub>, MXene, and NiMo<sub>3</sub>S<sub>4</sub>-MXene catalysts can be calculated by the following equation:

$$\text{ECSA} = \frac{C_{\text{dl}}}{C_s} \quad (9)$$

To calculate *C*<sub>dl</sub>, a series of CV curves under alkaline conditions were obtained at multiple scan rates in the non-faradaic region (Fig. S5a and b†). Fig. 5c shows plots of Δ*j* as a function of a scan rate that yields a straight line whose slope is taken as *C*<sub>dl</sub>. The specific capacitance (*C*<sub>s</sub>) was ~35 μF cm<sup>-2</sup> based on variously reported capacitances of metal-based electrodes in alkaline solutions.<sup>40</sup> NiMo<sub>3</sub>S<sub>4</sub>-MXene exhibited a relatively higher *C*<sub>dl</sub> (60.83 μF cm<sup>-2</sup>), greater than those of MXene (47.63 μF cm<sup>-2</sup>), and NiMo<sub>3</sub>S<sub>4</sub> (22.38 μF cm<sup>-2</sup>). As a result, the ECSA of NiMo<sub>3</sub>S<sub>4</sub>-MXene, MXene, and NiMo<sub>3</sub>S<sub>4</sub> was calculated to be 1.73 cm<sup>2</sup>, 1.36 cm<sup>2</sup>, and 0.31 cm<sup>2</sup>, respectively, indicating that due to its high conductivity, NiMo<sub>3</sub>S<sub>4</sub>-MXene had the highest exposure of effective active sites, which enhanced its contact with the electrolyte. Surface topology can influence catalyst performance, so LSV data were normalized by the ECSA to determine the intrinsic HER activity of each catalyst, as presented in Fig. 5d. A similar trend of catalytic activity for these three electrocatalysts compared with the geometric area-normalized LSV curves (presented in Fig. 5a) was observed. The ECSA of NiMo<sub>3</sub>S<sub>4</sub> was significantly enhanced upon forming its hybrid with MXene. Hence, its electrocatalytic performance was attributed to a synergistic effect arising from the high ECSA of MXene and superior catalytic performance of NiMo<sub>3</sub>S<sub>4</sub>. These

findings are in line with the literature, which highlights the prominent effect of ECSA on HER activity and kinetics.<sup>41</sup>

EIS was carried out for the measurement of the electrochemical impedance and electron transfer properties of the prepared electrode material in frequency range of 100 kHz to 0.01 Hz. EIS results and the equivalent circuit-fitting model are presented in Fig. 6. Pristine NF was best fitted with the CPE circuit model. The obtained Nyquist plots of all electrocatalysts were best fitted to a contact phase element (CPE) with a diffusion-equivalent circuit model. An equivalent circuit was presented that is consist of a reference electrode (R.E.), along with the solution resistance (*R*<sub>s</sub>), which represents the resistance of the electrolyte. *Y*<sub>0</sub> denotes CPE admittance, and *W*<sub>d</sub> is the Warburg element, which represents the diffusion or mass transport resistance. Additionally, the circuit included the charge transfer resistance (*R*<sub>ct</sub>) and working electrode (W.E.), reflecting the interfacial electrochemical dynamics at the electrode surface. The relevant parameters are summarized in ESI as Table S1.† Information about the *R*<sub>s</sub> of electrode materials as well as the *R*<sub>ct</sub> corresponded to the electrocatalytic kinetics at the electrode/electrolyte interface (Fig. 5). All electrocatalysts experienced an *R*<sub>s</sub> value close to each other, but a significant difference in their *R*<sub>ct</sub> values was observed. The estimated *R*<sub>ct</sub> for NiMo<sub>3</sub>S<sub>4</sub>, MXene, and NiMo<sub>3</sub>S<sub>4</sub>-MXene was 11.06 Ω, 2.84 Ω, and 2.18 Ω, respectively. The smallest value for NiMo<sub>3</sub>S<sub>4</sub>-MXene indicated a fast electrocatalytic process and, therefore, superior HER kinetics. The low charge transfer resistance of NiMo<sub>3</sub>S<sub>4</sub>-MXene revealed that the hybrid structure had a key role in electrocatalytic performance. The synergistic effect in NiMo<sub>3</sub>S<sub>4</sub>-MXene arises from the excellent electrocatalytic activity of NiMo<sub>3</sub>S<sub>4</sub> and high conductivity of MXene, which collectively offered higher water oxidation and efficient charge transfer, thereby improving the overall performance.<sup>42</sup> A summary of the HER kinetics of designed electrocatalysts is given in Table 1.

The stability of all prepared electrocatalysts was evaluated by performing 1000 CV cycles at a scan rate of 50 mV s<sup>-1</sup> for the HER in 1.0 M KOH electrolyte (Fig. S6†). The electrodes were pre-activated by immersion in an electrolyte solution for 1 h,

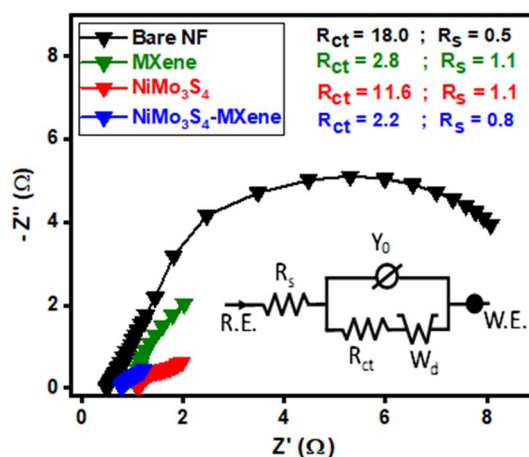
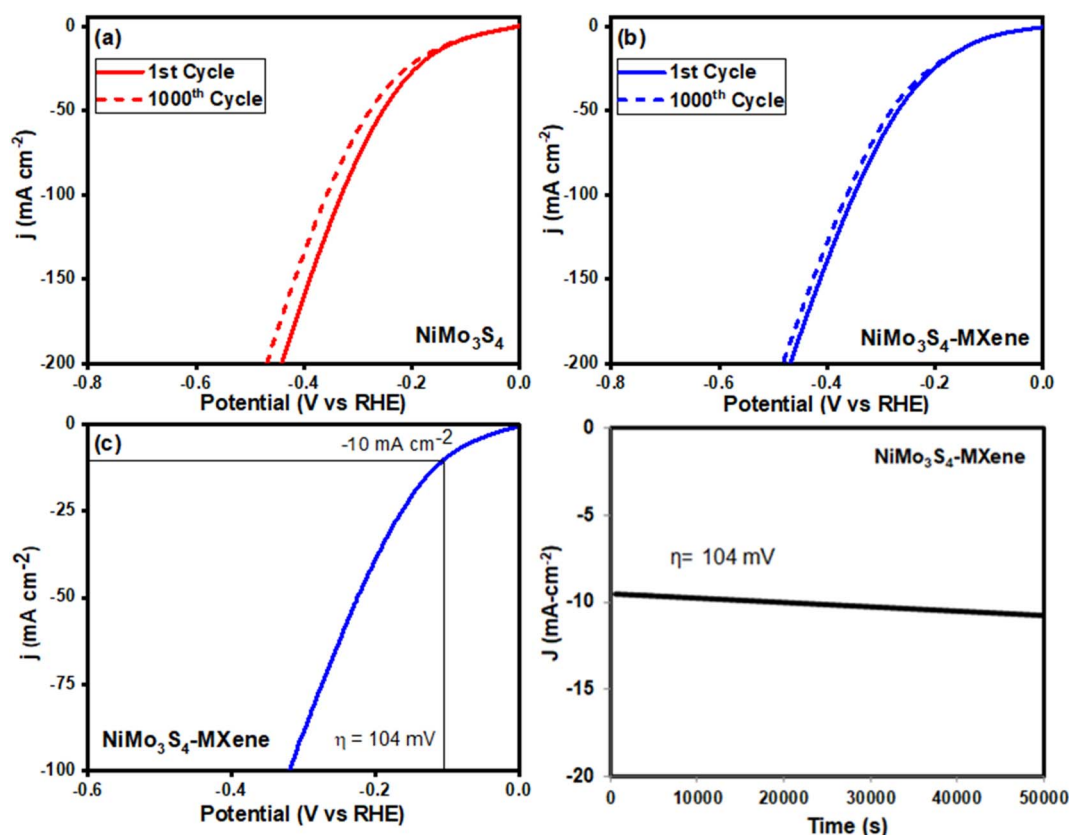


Fig. 6 Nyquist plot of bare Ni-foam, MXene, NiMo<sub>3</sub>S<sub>4</sub>, and NiMo<sub>3</sub>S<sub>4</sub>-MXene measured at a potential of −0.2 V vs. RHE (the unit of *R*<sub>ct</sub> and *R*<sub>s</sub> values is Ω).



Table 1 HER performances of prepared electrocatalysts in 1 M KOH

Electrodes	Onset potential (mV)	$\eta_{10}$ (mV)	Tafel slope (mV dec <sup>-1</sup> )	$C_{dl}$ ( $\mu\text{F cm}^{-2}$ )	$R_{ct}$ (ohm)	$R_s$ (ohm)
NF	106	397	115	0.94	18	0.5
MXene	46	287	98	47.63	2.84	1.08
NiMo <sub>3</sub> S <sub>4</sub>	33	241	68	22.38	11.06	1.12
NiMo <sub>3</sub> S <sub>4</sub> -MXene	21	104	52	60.83	2.18	0.8

Fig. 7 LSV curves of electrocatalysts before and after 1000 cycles. (a) NiMo<sub>3</sub>S<sub>4</sub> and (b) NiMo<sub>3</sub>S<sub>4</sub>-MXene. (c) LSV of NiMo<sub>3</sub>S<sub>4</sub>-MXene and (d) chronoamperometry data of NiMo<sub>3</sub>S<sub>4</sub>-MXene.

followed by 50 cycles of CV prior to recording data for the stability test. After activation, the initial LSV scan was recorded. Subsequently, another LSV scan was conducted after 1000 cycles, and the resulting polarization curves were compared, as shown in Fig. 7a and b. The LSV curve of NiMo<sub>3</sub>S<sub>4</sub> before and after 1000 cycles of CV showed slight loss of performance as the overpotential at a certain current density increased after running 1000 cycles. However, this performance loss significantly diminished after formation of the composite of NiMo<sub>3</sub>S<sub>4</sub> with MXene. This finding indicated that the *in situ* synthesis of NiMo<sub>3</sub>S<sub>4</sub> covered the surface of MXene 2D nanosheets, preventing the restacking of MXene layers and preventing MXene from oxidation because no oxides of titanium were observed in EDX analysis. Additionally, the interaction between NiMo<sub>3</sub>S<sub>4</sub> with MXene after hybrid formation improved the stability and preserved the active sites for long-term use to perform electrocatalytic reactions.

The stability of the NiMo<sub>3</sub>S<sub>4</sub>-MXene electrode was further evaluated using chronoamperometry at a constant potential of 104 mV (corresponding to a current density of approximately  $-10 \text{ mA cm}^{-2}$ ) in 1.0 M KOH for  $\sim 14$  h, as shown in Fig. 7(c), with the results displayed in Fig. 7(d). Following a slight initial drop (likely due to temporary blockade of active sites by accumulated hydrogen bubbles), the current density remained stable or slightly increased over time. Continuous stirring helped release the bubbles, keeping the active sites accessible for the reaction. Overall, NiMo<sub>3</sub>S<sub>4</sub>-MXene demonstrated excellent stability over the 14 h testing period.

The overpotential of NiMo<sub>3</sub>S<sub>4</sub>-MXene compared with other MXene-based hybrid electrocatalysts reported in the literature is presented in Fig. 8, and the comparison is summarized in Table S2.† NiMo<sub>3</sub>S<sub>4</sub>-MXene outperformed several competing structures, making it a promising candidate for the HER in



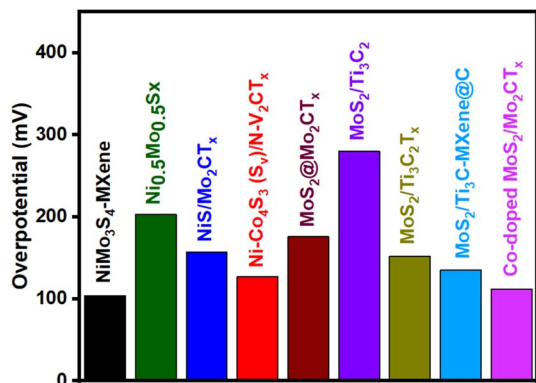


Fig. 8 Comparison of the overpotential of NiMo<sub>3</sub>S<sub>4</sub>-MXene (at a current density of 10 mA cm<sup>-2</sup>) with some relevant materials reported in the literature.<sup>26,43–48</sup>

alkaline media, with notably low overpotential (104 mV) at current density of 10 mA cm<sup>-2</sup>.

## 4 Conclusions

The NiMo<sub>3</sub>S<sub>4</sub>-MXene hybrid electrocatalyst was synthesized *via* a facile hydrothermal method. Electrochemical studies revealed that NiMo<sub>3</sub>S<sub>4</sub>-MXene exhibited remarkably good performance, with quite low overpotential (104 mV) and Tafel slope of 52 mV dec<sup>-1</sup>. The NiMo<sub>3</sub>S<sub>4</sub>-MXene hybrid electrocatalyst also demonstrated excellent conductivity, with charge transfer resistance of 2.18 Ω. This excellent performance of NiMo<sub>3</sub>S<sub>4</sub>-MXene was attributed to the synergistic effect between NiMo<sub>3</sub>S<sub>4</sub> and MXene, whereby NiMo<sub>3</sub>S<sub>4</sub> contributes to high electrocatalytic activity, and MXene provides a large 2D surface area, promoting high-quality hybrid formation and enhanced conductivity. The highest ECSA of NiMo<sub>3</sub>S<sub>4</sub>-MXene indicated greater exposure of active sites, allowing efficient diffusion of the electrolyte into the electrode material and enabling a conductive pathway for electron transfer between MXene sheets. Our results demonstrated that the transition-metal chalcogenides, if coupled with MXene, showed significantly improved electrochemical performance due to higher conductivity, lower charge transfer resistance, larger ECSA, and excellent cyclic stability. NiMo<sub>3</sub>S<sub>4</sub>-MXene is a promising candidate for the HER, and other transition-metal chalcogenides can be explored in combination with 2D nanomaterials to enhance the electrocatalytic performance used in large-scale hydrogen production.

## Data availability

The data obtained from our study can be provided upon reasonable demand.

## Author contributions

Shaista Zubaid: conceptualization, data curation, methodology, investigation, visualization, validation, and writing (original

draft). Misbah Jabeen: conceptualization, data curation, methodology, and writing (original draft). Hirra Ahmad: data curation, investigation, methodology, software, and validation. Abid Ur Rehman Chaudhary: data curation, investigation, methodology, software, and validation. Syed Ali Raza Naqvi: investigation, methodology, software, and validation. Aliya Tufail: data curation, methodology, investigation, and software. Atta Ullah Shah: data curation, resources, investigation, and software. Yaqoob Khan: supervision, data curation, resources, investigation, and software. Tauqir A. Sherazi: conceptualization, funding acquisition, investigation, methodology, data curation, project administration, supervision, validation, visualization, and writing (review and editing).

## Conflicts of interest

The authors declare no competing financial interest.

## Acknowledgements

The authors gratefully acknowledge the financial support of the Higher Education Commission of Pakistan (20-3684/R&D/HEC/14) and Pakistan Science Foundation (PSF/NSFC-Eng/KP-COMSATs-ABT-04). Tauqir A. Sherazi acknowledges financial support from the Alexander von Humboldt Foundation.

## References

- 1 N. Yuan, Q. Jiang, J. Li and J. Tang, *Arabian J. Chem.*, 2020, **13**, 4294–4309.
- 2 S. Wang, A. Lu and C.-J. Zhong, *Nano Convergence*, 2021, **8**, 4.
- 3 S. N. Upadhyay and S. Pakhira, in *Photoelectrochemical Hydrogen Generation: Theory, Materials Advances, and Challenges*, ed. P. Kumar and P. Devi, Springer Nature Singapore, Singapore, 2022, pp. 59–89, DOI: [10.1007/978-981-16-7285-9\\_3](https://doi.org/10.1007/978-981-16-7285-9_3).
- 4 X. Li, L. Zhao, J. Yu, X. Liu, X. Zhang, H. Liu and W. Zhou, *Nano-Micro Lett.*, 2020, **12**, 131.
- 5 Y. Yang, K. Zhang, H. Lin, X. Li, H. C. Chan, L. Yang and Q. Gao, *ACS Catal.*, 2017, **7**, 2357–2366.
- 6 B. H. R. Suryanto, Y. Wang, R. K. Hocking, W. Adamson and C. Zhao, *Nat. Commun.*, 2019, **10**, 5599.
- 7 C. Li and J.-B. Baek, *ACS Omega*, 2020, **5**, 31–40.
- 8 T. Wu, M. Z. Sun and B. L. Huang, *Rare Met.*, 2022, **41**(7), 2169–2183.
- 9 H. Wu, C. Feng, L. Zhang, J. Zhang and D. P. Wilkinson, *Electrochem. Energy Rev.*, 2021, **4**(3), 473–507.
- 10 Z. D. Gul, S. Zubaid, A. Batool, Y. Khan and T. A. Sherazi, *Int. J. Hydrogen Energy*, 2024, **51**, 946–955.
- 11 W.-J. Jiang, T. Tang, Y. Zhang and J.-S. Hu, *Acc. Chem. Res.*, 2020, **53**, 1111–1123.
- 12 M. A. Younis, S. Lyu, Q. Zhao, C. Lei, P. Zhang, B. Yang, Z. Li, L. Lei, Y. Hou and X. Feng, *BMC Mater.*, 2019, **1**, 6.
- 13 S. Zubaid, J. Khan and T. A. Sherazi, *J. Colloid Interface Sci.*, 2024, **660**, 502–512.



- 14 S. Jabeen, T. A. Sherazi, R. Ullah, S. A. R. Naqvi, M. A. Rasheed, G. Ali, A. U. Shah and Y. Khan, *Appl. Nanosci.*, 2021, **11**, 79–90.
- 15 J. Qiao, L. Kong, S. Xu, K. Lin, W. He, M. Ni, Q. Ruan, P. Zhang, Y. Liu, W. Zhang, L. Pan and Z. Sun, *Energy Storage Mater.*, 2021, **43**, 509–530.
- 16 J. Liu, W. Peng, Y. Li, F. Zhang and X. Fan, *Trans. Tianjin Univ.*, 2020, **26**, 149–171.
- 17 S. Bai, M. Yang, J. Jiang, X. He, J. Zou, Z. Xiong, G. Liao and S. Liu, *npj 2D Mater. Appl.*, 2021, **5**, 78.
- 18 Y. Tang, C. Yang, X. Xu, Y. Kang, J. Henzie, W. Que and Y. Yamauchi, *Adv. Energy Mater.*, 2022, **12**, 2103867.
- 19 L. Tie, N. Li, C. Yu, Y. Liu, S. Yang, H. Chen, S. Dong, J. Sun, S. Dou and J. Sun, *ACS Appl. Energy Mater.*, 2019, **2**, 6931–6938.
- 20 J. Zhao, J. Wang, Z. Chen, J. Ju, X. Han and Y. Deng, *APL Mater.*, 2021, **9**, 050902.
- 21 Y. Xin, X. Kan, L.-Y. Gan and Z. Zhang, *ACS Nano*, 2017, **11**, 10303–10312.
- 22 J. Zhang, W. Zhang, J. Zhang, Y. Li, Y. Wang, L. Yang and S. Yin, *J. Alloys Compd.*, 2023, **935**, 167974.
- 23 J. Jiang, M. Gao, W. Sheng and Y. Yan, *Angew. Chem., Int. Ed.*, 2016, **55**, 15240–15245.
- 24 J. Ran, G. Gao, F.-T. Li, T.-Y. Ma, A. Du and S.-Z. Qiao, *Nat. Commun.*, 2017, **8**, 13907.
- 25 Y. Meng, C. Liang, D. Jiang, Y. Zhang, J. Su, X. Xu and M. Lu, *Chem. Eng. J.*, 2024, **479**, 147695.
- 26 L. Huang, L. Ai, M. Wang, J. Jiang and S. Wang, *Int. J. Hydrogen Energy*, 2019, **44**, 965–976.
- 27 M. Naguib, M. Kurtoglu, V. Presser, J. Lu, J. Niu, M. Heon, L. Hultman, Y. Gogotsi and M. W. Barsoum, *Adv. Mater.*, 2011, **23**, 4248–4253.
- 28 A. G. Juandito, D. S. Khaerudini, S. Priyono, G. T. Kadja, D. Djuhana and M. Khalil, *J. Nanopart. Res.*, 2024, **26**, 110.
- 29 A. C. Y. Yuen, T. B. Y. Chen, B. Lin, W. Yang, I. I. Kabir, I. M. De Cachinho Cordeiro, A. E. Whitten, J. Mata, B. Yu, H.-D. Lu and G. H. Yeoh, *Compos., Part C: Open Access*, 2021, **5**, 100155.
- 30 S. Luan, M. Han, Y. Xi, K. Wei, Y. Wang, J. Zhou, L. Hou and F. Gao, *Ionics*, 2020, **26**, 51–59.
- 31 M. Kumar, B. Ramulu and J. S. Yu, *Mater. Chem. Front.*, 2024, **8**, 1844–1851.
- 32 Q. Qin, L. Chen, T. Wei and X. Liu, *Small*, 2019, **15**, 1803639.
- 33 M. Cittadini, M. Bersani, F. Perrozzi, L. Ottaviano, W. Wlodarski and A. Martucci, *Carbon*, 2014, **69**, 452–459.
- 34 M. Khalil, M. Lesa, A. G. Juandito, A. R. Sanjaya, T. A. Ivandini, G. T. Kadja, M. H. Mahyuddin, M. Sookhakian and Y. Alias, *Mater. Adv.*, 2023, **4**, 3853–3862.
- 35 R. Hasanah, Y. Romdoni, V. Fauzia, A. Arifutzzaman, F. Hussin, M. K. Aroua and M. Khalil, *Mater. Res. Bull.*, 2025, 113514.
- 36 S. Yao, L. Xu, H. Qin, X. Ding, S. Zhao, Y. Ma, M. Cui, Q. Lv, J. Han and F. Song, *New J. Chem.*, 2024, **48**, 18437–18442.
- 37 F. Wang, Y. Zhu, L. Qian, Y. Yin, Z. Yuan, Y. Dai, T. Zhang, D. Yang and F. Qiu, *Food Chem.*, 2024, **459**, 140379.
- 38 S. Tang, Z. Zhang, L. Xu, H. Qin, J. Dong, Q. Lv, J. Han and F. Song, *J. Colloid Interface Sci.*, 2024, **669**, 228–235.
- 39 T. Shinagawa, A. T. Garcia-Esparza and K. Takanabe, *Sci. Rep.*, 2015, **5**, 13801.
- 40 C. C. McCrory, S. Jung, J. C. Peters and T. F. Jaramillo, *J. Am. Chem. Soc.*, 2013, **135**, 16977–16987.
- 41 S. I. P. Bakovic, P. Acharya, M. Watkins, H. Thornton, S. Hou and L. F. Greenlee, *J. Catal.*, 2021, **394**, 104–112.
- 42 A. Patra, R. Samal and C. S. Rout, *Catal. Today*, 2023, **424**, 113853.
- 43 C. V. Inocêncio, J. Rousseau, N. Guignard, C. Canaff, S. Morisset, T. W. Napporn, C. Morais and K. B. Kokoh, *Int. J. Hydrogen Energy*, 2023, **48**, 26446–26460.
- 44 N. Wu, J. Liu, W. Zhao, J. Du and W. Zhong, *Int. J. Hydrogen Energy*, 2023, **48**, 17526–17535.
- 45 Y. Zhou, Y. Wu, D. Guo, J. Li, G. Dong, D.-F. Chai, X. Yang, S. Fu and G. Sui, *Mater. Chem. Front.*, 2023, **7**, 306–314.
- 46 J. Ren, H. Zong, Y. Sun, S. Gong, Y. Feng, Z. Wang, L. Hu, K. Yu and Z. Zhu, *CrystEngComm*, 2020, **22**, 1395–1403.
- 47 J. Liu, Y. Liu, D. Xu, Y. Zhu, W. Peng, Y. Li, F. Zhang and X. Fan, *Appl. Catal., B*, 2019, **241**, 89–94.
- 48 J. Liang, C. Ding, J. Liu, T. Chen, W. Peng, Y. Li, F. Zhang and X. Fan, *Nanoscale*, 2019, **11**, 10992–11000.

